J. Fluid Mech. (1997), *vol.* 338, *pp.* 35–58

Laboratory studies of equatorially trapped waves using ferrofluid

By DANIEL R. OHLSEN[1] AND PETER B. RHINES[2]

[1] Program in Atmospheric and Oceanic Sciences, University of Colorado, Boulder, CO 80309-0311, USA

[2] School of Oceanography, University of Washington, Seattle, WA 98195, USA

(Received 24 June 1994 and in revised form 12 July 1996)

We introduce a new technique to model spherical geophysical fluid dynamics in the terrestrial laboratory. The local vertical projection of planetary vorticity, f, varies with latitude on a rotating spherical planet and allows an important class of waves in large-scale atmospheric and oceanic flows. These Rossby waves have been extensively studied in the laboratory for middle and polar latitudes. At the equator f changes sign where gravity is perpendicular to the planetary rotation. This geometry has made laboratory studies of geophysical fluid dynamics near the equator very limited. We use ferrofluid and static magnetic fields to generate nearly spherical geopotentials in a rotating laboratory experiment. This system is the laboratory analogue of those large-scale atmospheric and oceanic flows whose horizontal motions are governed by the Laplace tidal equations. As the rotation rate in such a system increases, waves are trapped to latitudes near the equator and the dynamics can be formulated on the equatorial β-plane. This transition from planetary modes to equatorially trapped modes as the rotation rate increases is observed in the experiments. The equatorial β-plane solutions of non-dispersive Kelvin waves propagating eastward and non-dispersive Rossby waves propagating westward at low frequency are observed in the limit of rotation fast compared to gravity wave speed.

1. Introduction

Large-scale motions of both the atmosphere and ocean are nearly in vertical hydrostatic balance and horizontal geostrophic balance. The equator is a singular latitude where geostrophy breaks down since the vertical planetary vorticity there goes to zero. This change in sign of the Coriolis parameter with latitude gives rise to well-known classes of waves trapped to latitudes near the equator (see for example Gill 1982, chap. 11 or Philander 1990, chap. 3). These waves in both the atmosphere and ocean and their nonlinear interactions with mean flows and each other appear to play an important role in the Earth's climate system through the El Niño–Southern Oscillation phenomena.

Motivated by the early work of G. I. Taylor (1921), the understanding of much of geophysical fluid dynamics has progressed by a cross-fertilization between analytic, laboratory, and now numerical studies. Analytic equatorial β-plane and equatorial or fully spherical numerical models of the equatorial latitudes in both the ocean and atmosphere have successfully simulated many of the observed flows in the real Earth system (Philander 1990). As usual, such models are particularly adept at linear or weakly nonlinear flows. Laboratory studies of equatorial geophysical fluid dynamics

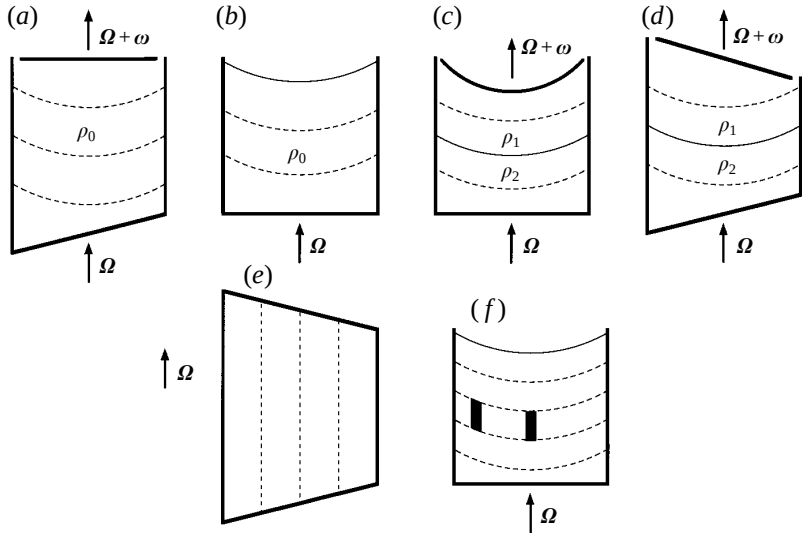

FIGURE 1. Various configurations of laboratory experiments relating to the β-effect, with equipotential surfaces dashed and fluid interfaces or free surfaces, solid lines. (*a*) Homogeneous fluid, sloping bottom and rigid top to give mid-latitude β. (*b*) Homogeneous fluid, horizontal bottom and parabolic free surface to give polar β. (*c*) Two immiscible fluids ($\rho_2 > \rho_1$), horizontal bottom, rigid parabolic lid of twice the fluid interface curvature to give baroclinic polar β. (*d*) Two fluids ($\rho_2 > \rho_1$), sloping bottom and top to give mid-latitude baroclinic β. (*e*) Weak stratification (dashed lines) and extremely fast rotation to give equatorial f-plane. (*f*) Continuous stratification (dashed lines), flat bottom and free surface has no internal potential vorticity gradient (bold vertical columns all have the same height) so only the barotropic mode sees β as in (*b*) rather than a spectrum of internal baroclinic modes.

have been extremely limited. In particular, generation of a gravitational body force which is steady and perpendicular to the rotation vector in the rotating coordinate system has proved difficult, and generation of variations of the planetary vorticity with latitude in such a system, i.e. a β-plane, even more so.

Many laboratory studies of large-scale waves in rotating systems have been presented for mid-latitude and polar β-planes in one or two layers using topographic β-planes. The rotation, $\boldsymbol{\Omega}$, and gravitational acceleration, $\boldsymbol{g}$, vectors are made parallel to avoid oscillatory gravity in the rotating reference frame. This orientation requires that top and/or bottom topography or free-surface curvature be used to simulate a planetary vorticity gradient and therefore β via vortex stretching. Thus a gradient of potential vorticity within layers of constant density is generated by spatial variations in the depth of the layer rather than by variations in the planetary vorticity. Figure 1 shows some example geometries: (*a*) uniform-density barotropic Rossby waves in a 'sliced cylinder' or channel with a sloping bottom (Ibbetson & Phillips 1967; Greenspan 1968); (*b*) again uniform-density Rossby wave dynamics, and induced mean circulation using the paraboloidal free surface and flat bottom to provide a potential vorticity gradient (a 'polar β-plane', Whitehead 1975; Colin de Verdiere 1978), or source–sink-driven circulations in radial pie-shaped sections of such a cylinder with a free surface (Stommel, Arons & Faller 1958); (*c*) two layers of differing density, baroclinic wave dynamics and transition to chaos using a paraboloidal upper and flat lower boundary (Hart 1972; Ohlsen & Hart 1989); and (*d*) a two-layer density field and sloping plane upper and lower boundaries (Griffiths & Cornillon 1994).

When continuous density stratification is present in terrestrial laboratory exper-

iments, the mean state involves surfaces of constant pressure, density, and geopotential, Φ, which all coincide. Thus

$$\Phi = gz - \tfrac{1}{2}\Omega^2 r^2, \tag{1}$$

where $\Omega \equiv |\boldsymbol{\Omega}|$ is the experiment rotation rate, r is radial distance from the rotation axis, g is terrestrial gravity magnitude, and z is the local vertical coordinate. Assuming incompressibility, the potential vorticity, q, is

$$q = \frac{(2\boldsymbol{\Omega} + \boldsymbol{\omega}) \cdot \boldsymbol{\nabla}\rho}{\rho}, \tag{2}$$

where $\boldsymbol{\omega} = \boldsymbol{\nabla} \times \boldsymbol{u}$ is the relative vorticity, $\boldsymbol{u}$ is the velocity, and ρ is the density. The crucial limitation of the laboratory system is that the mean state field of q,

$$\bar{q} = \frac{2\boldsymbol{\Omega} \cdot \boldsymbol{\nabla}\rho}{\rho}, \tag{3}$$

is uniform in the absence of mean currents, i.e. $\bar{q}$ is proportional to $2\Omega/h$ where h is the z-separation of equipotential surfaces (figure 1*f*). Hence, neither baroclinic Rossby-wave dynamics, nor internal Sverdrup balance is possible.

A very limited set of equatorial flows has been modelled in the laboratory. Convection in very rapidly rotating cylindrical annuli (figure 1*e*) and spherical shells has been studied using centripetal acceleration to dominate terrestrial gravity (Carrigan & Busse 1983; Azouni, Bolton & Busse 1986). Their resultant 'gravity' is everywhere nearly perpendicular to the rotation vector to give near-equatorial dynamics. With respect to baroclinic flows this is an 'equatorial *f*-plane' because, again, the potential vorticity of the mean state is uniform on density surfaces. Barotropic motions (here influenced by sloping end caps, or spherical-shell geometry) see a β-effect, yet it is negative in the equatorial zone where thickness, measured parallel to $\boldsymbol{\Omega}$, decreases equatorward (poleward of the circumscribing cylinder in a spherical annulus, the thickness increases equatorward). These experiments have verified predictions of models of buoyancy-driven flows in giant-planet and stellar atmospheres and cores.

Some aspects of the barotropic oceanic general circulation in basins at various latitudes including the equator have been simulated in the laboratory using a rotating spherical shell of homogeneous fluid (Baker & Robinson 1969). Their model basin rigidly enclosed the fluid to eliminate terrestrial gravity from the dynamics, and flow was driven by differential rotation of one of the spherical shells. They observed subtropical gyre-like flow including Sverdrup flow, western boundary currents, and an undercurrent on the equator. In such a homogeneous fluid, strong rotation leads to Taylor–Proudman flows with fluid moving in columns parallel to $\boldsymbol{\Omega}$. Buoyancy effects so strongly inhibit the horizontal component of $\boldsymbol{\Omega}$ in stratified oceans and atmospheres that this rigid-column flow is not likely to be relevant. Terrestrial gravity required that both these laboratory flows have rigid lids and small or no vertical density gradient in order to ensure that the dominant body force is perpendicular to the rotation vector.

It is possible to eliminate terrestrial gravity altogether by placing an experiment in free-fall or Earth orbit. Convection in a rotating hemispherical shell was studied by Hart, Glatzmaier & Toomre (1986) aboard Spacelab 3 on the space shuttle Challenger. A strong electric field across the shell gave a radial body force in the dielectric fluid. Flow was forced by radial and latitudinal temperature gradients and a 'laboratory' model of giant-planet and stellar convection dynamics was realized. The geometry was a hemisphere with a no-slip boundary at the equator so some global but not equatorial flows could be observed. This apparatus does model the spherical and not just β-plane

geometry of planetary buoyancy-driven flows. In this paper, we present a related technique involving a magnetic body force acting on ferrofluid which yields a nearly spherical geometry. The work here is limited to a single homogenous fluid layer with a free surface, for the study of external-mode freely propagating planetary-scale and equatorial waves. We have produced a quasi-spherical fully stratified fluid version, which in principle allows the extension of this work to simulations of the fully stratified ocean and atmosphere. However, the stratified version is complicated by the presence of both magnetic and gravitational body forces as discussed in the conclusions below, and the full implementation of the stratified model has not yet been carried out.

Salby (1984) reviews the atmospheric observations and theory for planetary-scale waves. Recently Delcroix, Picaut & Eldin (1991) and Chelton & Schlax (1996) report satellite observations of Pacific sea surface height showing equatorially trapped Kelvin and Rossby waves. These observations motivate the present study. Much of the dynamics of large-scale horizontal wave propagation in both the stratified atmosphere and ocean can be well modelled with reduced-gravity shallow-water equations. For shallow-water flow on a rotating sphere, the horizontal equations are the Laplace tidal equations. To get these equations, the traditional approximation (Phillips 1966) is made in which two Coriolis terms are neglected, $w2\Omega\cos\theta$ in the x-momentum equation and $-u2\Omega\cos\theta$ in the z-momentum equation, where u, v, and w are the x-, y-, and z-components of velocity, Ω is the planetary rotation and θ is the latitude (e.g. Holton 1992). In doing so, one neglects moderate-aspect-ratio non-hydrostatic motions in which fluid velocities do not vary along lines parallel with the rotation axis (rather than being invariant in the local vertical direction). An example is the cylindrical shear layer that can form, circumscribing the inner solid boundary. Here we follow the traditional practice and neglect the possibility of such 'cylindrical' flows, though clearly they are possible in our experiments.

Longuet-Higgins (1968) has delineated the free-wave and forced solutions of the Laplace tidal equations as a function of the Lamb parameter,

$$\epsilon \equiv 4\Omega^2 R^2/c^2, \tag{4}$$

where R is the planetary radius, and c is the shallow-water gravity wave speed, $c = (gh)^{1/2}$. Baroclinic waves can also be included in this formulation using an equivalent depth, h_m, determined by their vertical structure with wavenumber m, and a resultant horizontal phase speed $c_m = (gh_m)^{1/2}$. The important large-scale equatorial oceanic or atmospheric flows that we would like to model in a laboratory experiment correspond to the limit of large ϵ. In this limit, wave energy is trapped at latitudes near the equator and the equations can be reformulated on an equatorial β-plane (Matsuno 1966). Barotropic ocean modes have a large phase speed of ~ 200 m s^{-1} and therefore $\epsilon \sim 22$ but baroclinic modes in the ocean have $c_m \lesssim 3$ m s^{-1} and therefore $\epsilon \gtrsim 10^5$. Similarly baroclinic waves in the equatorial atmosphere with $c_m \sim 50$ m s^{-1} have $\epsilon \sim 350$. In these experiments we achieve Lamb parameters from 0 (non-rotating) to ~ 320.

The Lamb parameter can be used to determine the relative horizontal scale of either midlatitude or equatorial wave disturbances compared to the planetary radius. Since the external or internal Rossby radius, $L_r = c/f$ or c_m/f respectively,

$$\epsilon = (R/L_r)^2. \tag{5}$$

Similarly, since the external or internal equatorial Rossby radius,

$$L_{eq} = (c/\beta)^{1/2} = (cR/2\Omega)^{1/2} \quad \text{or} \quad (c_m R/2\Omega)^{1/2},$$
$$\epsilon = (R/L_{eq})^4. \tag{6}$$

Thus a large Lamb parameter implies that the scale of motion of the waves becomes small compared to the planetary radius. Physically this means that the rotation timescale is small compared to the buoyancy timescale and the propagating waves must balance the Coriolis acceleration with latitudinal variations in velocity and height. These experiments demonstrate the predicted trapping of wave energy to equatorial latitudes for increasing ϵ, and the characteristic wave solutions for large ϵ (or equivalently, on the equatorial β-plane) are observed.

In §2 we briefly describe ferrofluids and reduce the equations of ferrohydrodynamics to our system of vertical hydrostatic and horizontal geostrophic balance. The apparatus is also described along with our method to eliminate terrestrial gravity from the wave dynamics. In §3 the experiment is scaled to the geophysical flows of interest. The solutions to the Laplace tidal equation and their transition to the equatorial β-plane are reviewed and compared to the experiments for increasing Lamb parameter. In §4 the observations of equatorially trapped waves are reported and compared to the predictions of the β-plane theory. In §5 we summarize the results of these experiments and give a number of ideas for additional equatorial and planetary flows which could be studied with this system.

2. Experiment description

We begin by showing that the superparamagnetic response of ferrofluids in applied static magnetic fields can be used to generate a nearly radial body force for the study of free-surface flows of geophysical and astrophysical interest. Ferrofluids are dilute suspensions of magnetic dipoles, in our case magnetite particles of order 10 nm diameter, suspended in water. A surfactant coating on the particles keeps them separate enough that thermal motions in the fluid are sufficient to overcome gravity and keep the dipoles in suspension. In this study the magnetic fields are stationary and the bulk fluid motion is slow compared to the time for magnetic fluid particles to rotate ($\lesssim 10^{-6}$ s). A microscopic magnetization, $\boldsymbol{M}$, is realized as the suspended dipoles line up in an applied magnetic field, $\boldsymbol{H}$, and the resultant $\boldsymbol{M}$ is parallel to $\boldsymbol{H}$. If $\boldsymbol{H}$ is uniform, the equal but opposite force on the many north and south poles yields no net body force. If, however, there is a gradient in applied field, there will be a systematic force owing to the slight but persistent correlation of field strength and pole sense. This suggests a body force proportional both to the gradient of field density and to the fluid magnetization.

The monographs by Rosensweig (1985) and Bashtovoy, Berkovsky & Vislovich (1988) give very detailed derivations for the equations of ferrohydrodynamics. For rotating, incompressible flows the continuity and momentum equations become

$$\boldsymbol{\nabla}\cdot\boldsymbol{u} = 0 \tag{7}$$

and

$$\frac{\partial \boldsymbol{u}}{\partial t} + \boldsymbol{u}\cdot\boldsymbol{\nabla}\boldsymbol{u} + 2\boldsymbol{\Omega}\times\boldsymbol{u} + \boldsymbol{\Omega}\times\boldsymbol{\Omega}\times\boldsymbol{x} = -\frac{\boldsymbol{\nabla}p^*}{\rho} + \frac{1}{\rho}\, M\boldsymbol{\nabla}H + \nu\nabla^2\boldsymbol{u} + \boldsymbol{g}, \tag{8}$$

where

$$p^* = p - \int_0^H \rho^2 \left[\frac{\partial(M/\rho)}{\partial\rho}\right]_{H,T} \mathrm{d}H. \tag{9}$$

Note that, following the discussion above, it is the gradient of the scalar, $H = |\boldsymbol{H}|$, that appears in the momentum balance. In these equations $\boldsymbol{u}$ is the velocity, p the thermodynamic pressure, ρ the density, ν the kinematic viscosity, $\boldsymbol{\Omega}$ the rotation, and the magnetization and fields are defined by

$$\boldsymbol{B} = \boldsymbol{H} + 4\pi\boldsymbol{M}, \tag{10}$$

where $\boldsymbol{H}$ is the magnetic field, $\boldsymbol{B}$ is the magnetic induction and $\boldsymbol{M}$ is the material magnetization. These quantities are related in the fluid by an equation of state, $M = M(H, \rho)$, where again $\boldsymbol{M}$ is assumed parallel to $\boldsymbol{H}$.

For an ideal monodisperse colloidal ferrofluid the magnetization obeys the Langevin relation

$$\frac{M}{M_s} = L(\alpha) \equiv \coth(\alpha) - \frac{1}{\alpha}, \tag{11}$$

where

$$\alpha = \frac{mH}{kT} \tag{12}$$

and m is the magnetic moment of the suspended magnetic particles, k is Boltzman's constant, and T is the temperature. The saturation magnetization $M_s = nm$, where n is the number of magnetic particles per unit volume. For a dilute suspension ferrofluid like this one, the last term in (9) can be neglected since (as shown approximately in figure 3*b* below) the magnetization increases linearly with density for constant field, H. In other words M and ρ both increase linearly with n for H constant. Equation (9) then becomes

$$p^* = p \tag{13}$$

(Rosensweig 1985; Bashtovoy *et al.* 1988).

Typical rare-earth permanent magnets have fields of order 3000 Gauss near their pole surfaces, and much stronger permanent magnets or electromagnets are readily available (up to 50 000 Gauss superconducting magnets, for example). For simple dipole shapes, the field strength falls to near zero in tens of centimetres so that gradients of 100 Gauss cm^{-1} are possible. For comparison, the Earth's field is nearly uniform on laboratory scales and of order 0.7 Gauss. Commercially available ferrofluids have saturation magnetization, $4\pi M_s$, as large as 500 Gauss. Thus these simple magnets and inexpensive ferrofluids lead to magnetic accelerations, $M\boldsymbol{\nabla}H/\rho$, which can far exceed $|\boldsymbol{g}|$. Ferrofluid is more dense than its carrier (in this case water) and therefore magnetic and gravitational acceleration normally act in combination. To get a geophysically interesting radial body force, we eliminate terrestrial gravity in favour of the magnetic force alone.

The experiment geometry is shown in figure 2. A neodymium–iron–boron magnet with a surface field of approximately 3000 Gauss is embedded in a ball of casting plaster of radius 5.7 cm and surrounded by a layer of ferrofluid. This arrangement is suspended by a Plexiglas rod in an oil/freon mixture inside a cylindrical container on a rotating table. The oil mixture is immiscible with the ferrofluid and consists of Dow Corning silicone oil of viscosity $0.05\,\mathrm{cm}^2\,\mathrm{s}^{-1}$ along with a small amount of dibromotetrafluoroethane (to increase the mixture density) to give a density of $1.0096\,\mathrm{g\,cm}^{-3}$ at $T = 21.0\,^{\circ}\mathrm{C}$. The ferrofluid is a water-based suspension of magnetite particles coated with a lignin surfactant provided by Intermagnetics General Corp. diluted with distilled water at a volume ratio of about 1:14 (ferrofluid:water) giving $\rho = 1.0097\,\mathrm{g\,cm}^{-3}$ at $T = 21.0\,^{\circ}\mathrm{C}$. The densities were then further tuned by adjusting the temperature of the apparatus since the expansion coefficient of the oil mixture is twice that of the ferrofluid. For the experiments of §§3 and 4, the densities are matched to better than $0.0001\,\mathrm{g\,cm}^{-3}$ giving a reduced gravity of less than $0.1\,\mathrm{cm\,s}^{-2}$, i.e. at least twenty times less than the magnetic acceleration at the ferrofluid surface, $M\boldsymbol{\nabla}H/\rho \approx 2$–$15\,\mathrm{cm\,s}^{-2}$ (derived below). In the photograph of figure 2(*b*), the densities are not well matched and the ferrofluid is significantly heavier than the oil mixture. The

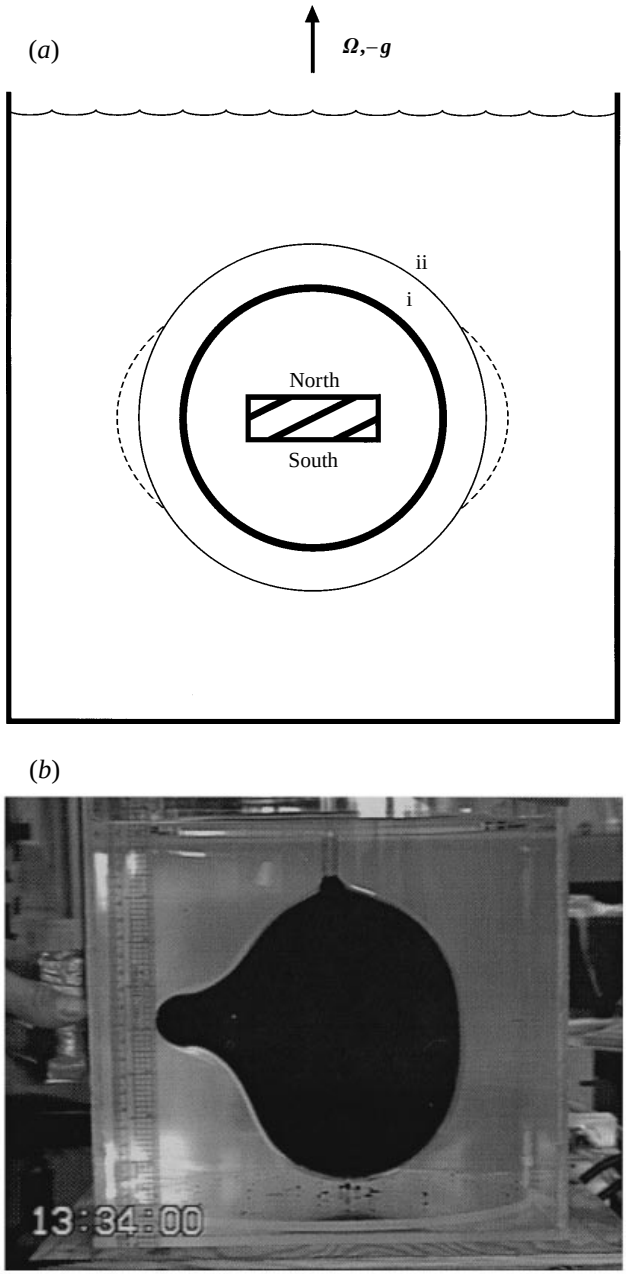

FIGURE 2. (*a*) Schematic cross-section of the axisymmetric experiment. A cylindrical tank holds a silicone oil – dibromotetrafluoroethane mixture (ii) surrounding a ferrofluid layer (i) on a plaster ball (whose surface is the thick circle) which surrounds a strong permanent magnet. The magnet poles are indicated by North and South for reference but the field line orientation is not important, only the field strength, $|\boldsymbol{H}|$, and its gradient, $\boldsymbol{\nabla} H$. The entire apparatus rotates at angular veocity, $\boldsymbol{\Omega}$. (*b*) Side view photograph of the laboratory experiment with an external magnet forcing a large-amplitude wave.

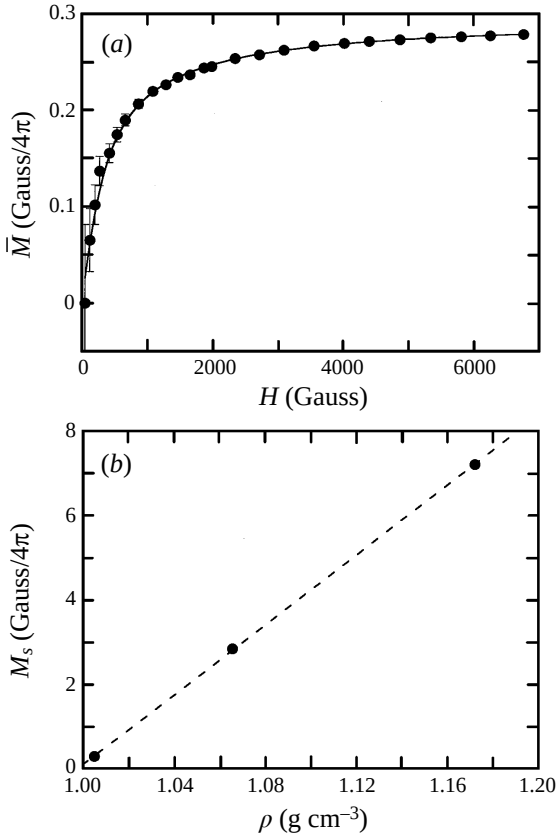

FIGURE 3. (*a*) $\bar{M}$ *vs.* magnetic field, H, for diluted ferrofluid sample measured via the modified Gouy method and a least-squares fit to (15). (*b*) Fit parameter M_S *vs.* density for three ferrofluid dilutions and a linear least-squares fit.

dilution ratio for the ferrofluid is a trade-off between making the magnetic body force and therefore the gravity wave speed small enough that the waves can be affected by the rotation while large enough that laboratory gravity can be ignored. Using this method, laboratory gravity is eliminated in favour of the magnetic body force.

Measurements of the field-averaged magnetization, $\bar{M}$, as a function of applied field, H, using the modified Gouy method (Rosensweig 1985) for a ferrofluid sample diluted with distilled water at about a 1:20 ratio are shown in figure 3(*a*) where

$$\bar{M} = \frac{1}{H}\int_0^H M \,\mathrm{d}H'. \tag{14}$$

A cylindrical volume of ferrofluid (with one end in a constant field region and the other in a field-free region) is weighed as a function of maximum field, H, and $\bar{M}$ is determined via the body force term, $M\nabla H$, in (8). The method is simple but less accurate than direct measurements of M with a vibrating sample magnetometer, for example. A fit to the integral of (11),

$$\bar{M} = M_s \frac{kT}{mH} \log\left[\frac{\sinh(mH/kT)}{mH/kT}\right], \tag{15}$$

with two free parameters, M_s and (kT/m), is shown and differs from the data due to

measurement errors in $\bar{M}$ at small H and to non-uniform magnetic particle size (Chantrell, Popplewell & Charles 1978). Similar measurements of $\bar{M}$ *vs.* H were made using the pure ferrofluid and less a diluted sample (about 1.6:1). The error-bars for $\bar{M}$ measurements are smaller for the less- and un-diluted ferrofluid samples and even better fits than shown in figure 3(*a*) are obtained. In figure 3(*b*) the saturation magnetization, M_s, obtained from the fits is plotted *vs.* ferrofluid density, ρ. A linear relationship between M_s and ρ is expected since $\rho = \rho_w + nm_p$, where ρ_w is the density of the water solvent and m_p is the magnetic particle mass, and, as mentioned above, $M_s = nm$. Indeed, data provided by Intermagnetics General Corp. show this linear relationship, and figure 3(*b*) verifies their measured slope. It remains then to design magnetic fields which give geophysically interesting geopotentials.

For an isothermal homogeneous ferrofluid the magnetic body force term in (8) $M\boldsymbol{\nabla}H = \boldsymbol{\nabla}\int_0^H M\,\mathrm{d}\boldsymbol{H}'$, and can therefore be absorbed into the pressure term. Without a free surface the ferrofluid flow is unaffected by magnetic fields, just as the interior of a homogeneous fluid is unaffected by gravity. For a basic resting state, (8) becomes

$$\rho\boldsymbol{\Omega}\times\boldsymbol{\Omega}\times\boldsymbol{x} = -\boldsymbol{\nabla}p + M\boldsymbol{\nabla}H + \rho\boldsymbol{g}, \tag{16}$$

and the general pressure boundary condition between a magnetic and a non-magnetic fluid is (Rosensweig 1985)

$$p^* + p_n = p_0 + p_c, \tag{17}$$

where $p_n \equiv 2\pi M_n^2$ is the magnetic normal traction in which M_n is the normal component of magnetization at the surface, p_0 is the static pressure on the non-magnetic side of the interface, and p_c is the capillary pressure. The attraction of ferrofluid to a magnet by the orientation of its microscopic dipoles requires, in equilibrium, a pressure gradient, and for this reason the pressure is lower on the ferrofluid side of an interface with non-ferrofluid. Bashtovoy *et al.* (1988, pp. 39–40) gives a nice explanation of this pressure jump, p_n, as the limit of the $M\boldsymbol{\nabla}H$ force changing at the free interface across an infinitesimal layer.

Since the density is uniform throughout the fluids, we subtract out, in the usual manner, the resting pressure p_0 which balances the gravitational and centripetal forces to get a hydrostatic equation for the magnetic fluid,

$$\frac{\partial p_m}{\partial z} = M\frac{\partial H}{\partial z}, \tag{18}$$

where z is the local vertical defined as anti-parallel to the gradient of the magnetic field strength, $p_m = p^* + p_n$, and p_c is neglected assuming that surface curvatures will be small. In the absence of laboratory gravity and the magnetic normal traction, p_n, eqns (18) and (13) would imply that the surfaces of constant magnetic field strength become the geopotentials for the fluid. To account for p_n we use the ferrohydrodynamic Bernoulli equation (Rosensweig 1985). For this constant-density resting state, the Bernoulli equation becomes

$$p - \int_0^H M\,\mathrm{d}H' = \text{constant} \tag{19}$$

where (13) has been used. For two points a and b on the fluid interface, (19) implies

$$p_a - \int_0^{H_a} M\,\mathrm{d}H' = p_b - \int_0^{H_b} M\,\mathrm{d}H'. \tag{20}$$

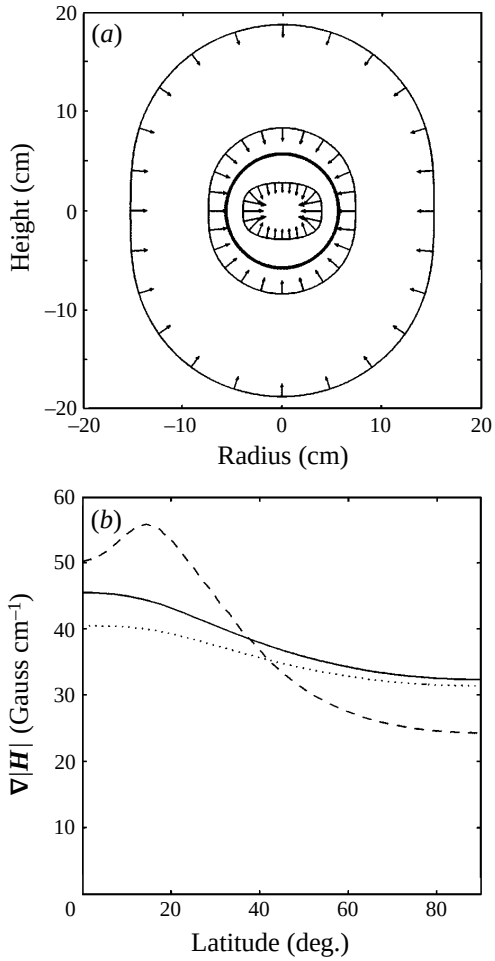

FIGURE 4. (*a*) Calculated axisymmetric contours of $|\boldsymbol{H}|$ and gradient $\nabla|\boldsymbol{H}|$ around the plaster ball. The contour levels are 5, 100, and 2000 Gauss. The gradient arrows also scale by factors of 20 between contours. (*b*) The magnitude of $\nabla|\boldsymbol{H}|$ as a function of latitude along the contours in (*a*). – – –, Gradient along the 2000 Gauss contour $\div 20$; ——, gradient along the 100 Gauss contour; · · ·, gradient along the 5 Gauss contour $\times 20$.

Using the boundary condition in (17), the definition of p_n, and the definition of $\overline{M}$ in (14), this becomes

$$2\pi M_{n_a}^2 + \overline{M}_a H_a = 2\pi M_{n_b}^2 + \overline{M}_b H_b. \tag{21}$$

Strictly speaking then, the fluid interface cannot be a surface of constant H since M_n varies with latitude on such a surface. However, since the field strength is very much larger than the magnetization for this dilute ferrofluid,

$$\overline{M}_a H_a \approx \overline{M}_b H_b, \tag{22}$$

and the magnetic field strength is very nearly constant on the interface. Equation (20) then implies that the interface does effectively lie on a geopotential given by a surface of constant magnetic field strength, since it is a surface of constant pressure.

The neodymium–iron–boron magnet is nearly rectangular, $6.5 \times 4.7 \times 2.0$ cm thick, magnetized in the short direction. Contours of magnetic field strength, $|\boldsymbol{H}|$, are shown in figure 4(*a*), calculated by simulating the magnet as a large number of axisymmetric

thin circular current loops. The experimental field was measured as a function of radius at both of the poles and at the equator at four meridians to constrain the calculation. The rectangular rather than cylindrical shape of the magnet means that longitude variations of the magnetic field and therefore 'gravity' are expected. These variations were observed to fall off quickly with distance. In addition the measurements show that the plaster ball is not quite centred on the dipole magnet. The effects of both on the wave speed with longitude are discussed below. The calculations in figure 4 assume cylindrical axisymmetry. Note that far from the magnet, the field falls off as a classic dipole and the potentials

$$|\boldsymbol{H}| \propto \frac{(3\cos^2\theta + 1)^{1/2}}{r^3}, \tag{23}$$

where r is the distance from the dipole centre and θ is the latitude.

A non-geophysical effect of this 'magnetic gravity' is that the magnitude and direction of the gradient of the magnetic field (and thus the force) are latitude dependent. This dependence is shown in figure 4(*a*) and detailed in figure 4(*b*) which shows the magnitude of the field gradient, $\boldsymbol{\nabla}|\boldsymbol{H}|$, as a function of latitude along the three geopotentials of figure 4(*a*). Note that the innermost curve has a gradient maximum off the equator, near the corner of the magnet. Near the magnet, the potentials are oblate, while far away they are prolate as in (23). The magnet diameter-to-height aspect ratio and plaster sphere size (dark circle in figure 4*a*) were chosen so that the ferrofluid surface for each of the three depths used is near the centre contour in figure 4(*a*) and has gradients shaped like the centre curve in figure 4(*b*). This is a trade-off between sufficiently large gradient and magnetic forces which are nearly spherically directed with small latitudinal amplitude variation. Finally, a topographic β-effect from (3) is present in the experiment owing to the latitudinal variation of the fluid layer depth. This effect will be relatively small in the equatorial region, and we neglect it.

The experimental set-up is sketched in figure 2. Waves on the surface of the ferrofluid are observed in profile by viewing the limb of the black ferrofluid spheroid against a white background. The equator ($\pm 90°$ longitude plane) can be observed from the bottom (side) using folded optics on the rotating table. The cylindrical Plexiglas container of oil is surrounded by a square water bath for optical correction of the side view. The index of refraction difference between the oil and water bath and the cylinder curvature combine to give a focal length of about 190 cm so that, viewed from this distance, the side view profile is indeed a plane that pierces the centre of the ferrofluid spheroid perpendicular to the viewing direction. The bottom view through a flat plate from a distance of about 220 cm is not corrected in the same way and thus the profile corresponds to 3–4° south latitude depending on the ferrofluid depth. It will turn out that both the amplitude and latitudinal extent of the waves are large enough that this error is unimportant.

In the side-view photograph of figure 2(*b*), a very strong dipole magnet external to the fluid tanks is attracting the ferrofluid away from around the plaster ball. The very black ferrofluid limits measurements of wave height to profile views. Obviously, very large-amplitude waves can be generated. The forcing is nonlinear, increasing quickly with decreasing distance (i.e. $\boldsymbol{\nabla}$ {equation (23)}) and depends intimately on the shape of the imposed magnetic field and therefore on the size and aspect ratio of the forcing magnet. For the following experiments, waves were generated by traversing the forcing magnet in a straight line (along the square optical tank) at constant speed and height in either the co-rotating direction (eastward) or counter-rotating (westward) direction.

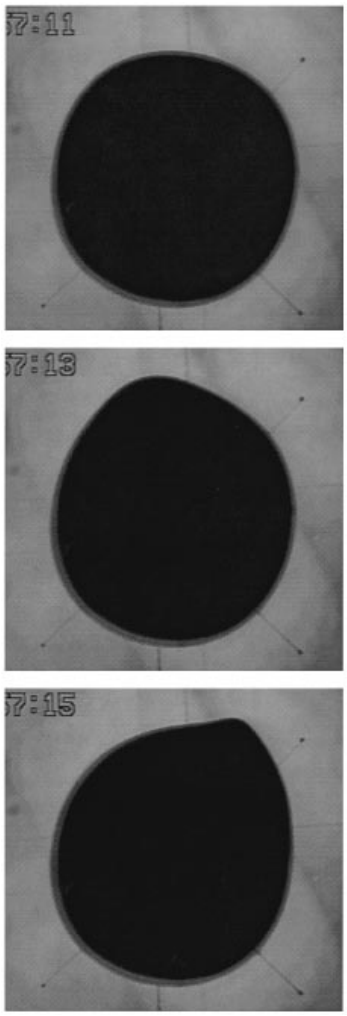

FIGURE 5. Sequence of south polar views of a wave on the ferrofluid spheroid. The wave is forced by an external magnet travelling in a straight line parallel to the tops of the images. The three protruding wires serve as image registration points for the video processing. The numbers count time in seconds.

An example polar view of such a wave is shown in the sequence of images in figure 5. The external magnet moves along the top of the images from left to right. The forced displacement height is symmetric in latitude about the equator with an approximately Gaussian shape as discussed in §4.

3. Geophysical scaling

To first approximation, planetary-scale fluid dynamics consists of vertical hydrostatic balance and horizontal geostrophic balance. This ferrofluid experiment has also been scaled to obey similar dynamics. The radii of the ferrofluid surface in the three different depth experiments are 6.4, 7.2, and 8.5 cm, giving average fluid depths of 0.7, 1.5, and 2.8 cm. The waves are forced to amplitudes of about 1–2 cm and then allowed to decay to zero. The horizontal (meaning along the magnetic geopotentials) scale is larger than either wave height or fluid depth, since the excited waves have zonal

wavenumber of order 3 or less. For these long waves and fluid depths $D \leqslant 0.1\lambda$ so the shallow-water approximation is appropriate. Comparing (17) to the usual derivation of shallow-water wave equations (for example, Gill 1982, §5.6), the term $M\partial H/\partial z$ serves as the gravity restoring force, $\rho\,\partial\Phi/\partial z = \rho g$. An interesting difference is that this force cannot be treated as independent of height as is normally done with g for atmospheric and oceanic flows.

Again using the Bernoulli equation (19) but for points a and b located on the plaster ball and the interface respectively,

$$p_a - \int_0^{H_a} M\,\mathrm{d}H' = p_b - \int_0^{H_b} M\,\mathrm{d}H'. \tag{24}$$

Still neglecting p_c in the boundary condition (17), these give

$$\begin{aligned} p_b = p_m &= -p_n + \int_{H_a}^{H_b} M\,\mathrm{d}H' \\ &= -p_n - \int_0^{D} M\frac{\mathrm{d}H}{\mathrm{d}z}\,\mathrm{d}z'. \end{aligned} \tag{25}$$

As shown above, the magnetic normal traction term is small, and near the equator, where this study will focus, $\boldsymbol{M}$, parallel to $\boldsymbol{H}$, is oriented north–south, and M_n and therefore $p_n \approx 0$ and will be ignored. Following the usual procedure for small surface displacements, η, about the resting depth, D, the perturbation pressure, p', is depth independent in the hydrostatic approximation, and

$$p' = M_D(\boldsymbol{\nabla}H)_D\,\eta, \tag{26}$$

where the subscript means the quantities are evaluated at height D above the plaster ball. Thus correspondence to the usual shallow-water formulation is obtained with the substitution of $M_D(\boldsymbol{\nabla}H)_D$ for $\rho\boldsymbol{g}$. In particular, the wave phase speed becomes

$$c = (M_D(\boldsymbol{\nabla}H)_D\,D/\rho)^{1/2}. \tag{27}$$

Note that the very strong magnet required a large ferrofluid dilution in order to give a sufficiently small magnetic force and therefore wave phase speed for equatorially trapped waves. This dilution had the further advantage of reducing the viscosity of the ferrofluid to approximately that of water, ~ 0.01 cm^2 s^{-1}.

An example of waves on the ferrofluid surface with no rotation ($\Omega = 0$) is shown in figure 6(*a*). The video camera view was of the south pole of the ferrofluid spheroid as in figure 5. The forcing magnet moved in a straight horizontal line in the equatorial plane along the flat optical box wall at a constant speed in first the westward and then eastward direction. High-resolution video tape images were frame-grabbed to computer memory at 0.3 s intervals as 8-bit intensity greyscales, and then the edge is found via a contour routine. This nearly circular edge is converted to polar coordinates and displayed as a radial displacement, $\eta = r - r_0$, at each longitude *vs.* time where r_0 is the motionless average radius at each longitude from the first four images. The resolution of this height-finding method is 0.1 pixel which is 3.7×10^{-3} cm for this shallow depth case. Longitude $-90°$ corresponds to the longitude of closest approach of the forcing to the ferrofluid spheroid. Note that the maximum amplitude of the forced wave occurs about 10° after the closest approach position due to the nonlinear ferrofluid response. The wave then freely propagates and decays. The zonal wave speed near the equator is roughly constant with longitude in figure 6(*a*) and is the same in either direction, as expected for the non-rotating case. These waves are not confined to

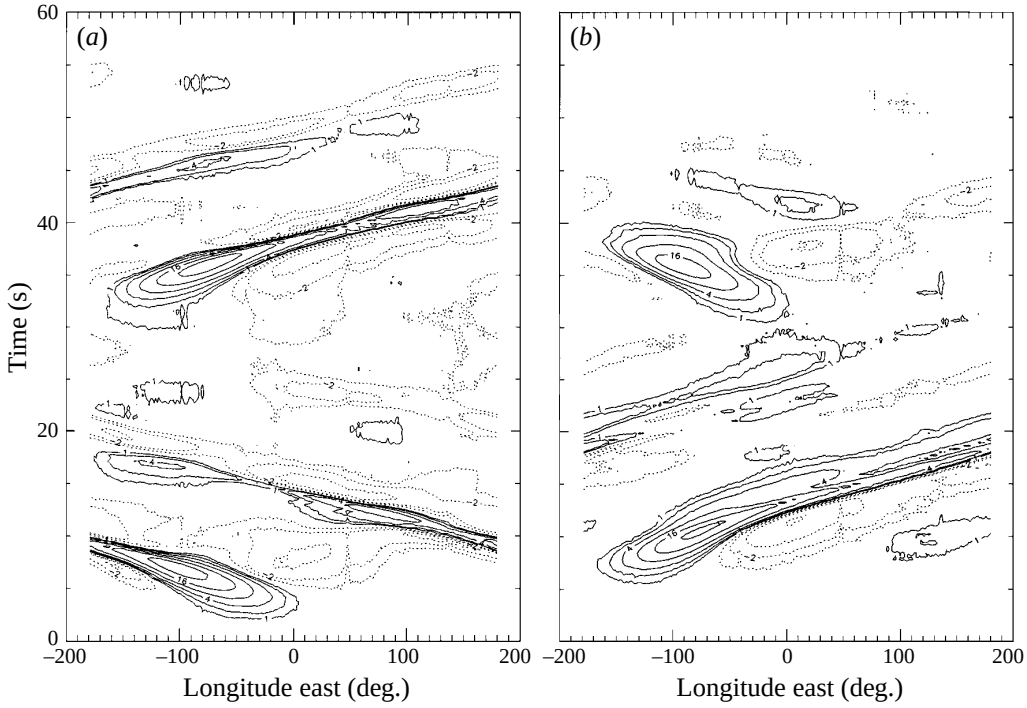

FIGURE 6. Contours of displacement height, $r-r_0$, near equator for shallow depth case as a function of longitude and time. The video frames of the south polar view are grabbed at 0.3 s intervals. Contours asre shown at $\pm 1, \pm 2, \pm 4, \pm 8, \ldots$ pixels with 1 pixel = 0.037 cm depth. (*a*) $\Omega = 0$, r_0 is the average of the first four images. At $t \approx 2$ s westward forcing, at $t \approx 30$ s eastward forcing. (*b*) $\Omega = 2.0\ \mathrm{s}^{-1}$, $\epsilon_m = 39$, r_0 is the average of the first ten images. At $t \approx 5$ s eastward forcing, at $t \approx 30$ s westward forcing.

the 'tropics' but were observed to propagate over the entire fluid spheroid. The increase in wave amplitude near longitude $+90°$ is a consequence of constructive interference of ray paths around the equator and over the poles.

With the addition of rotation, the wave motions are no longer symmetric in the eastward (co-rotating) and westward (counter-rotating) directions. In figure 6(*b*) $\Omega = 2.0\ \mathrm{s}^{-1}$ and the eastward wave propagates freely while the westward wave does not. The forcing speed is tuned to be about that of the expected eastward Kelvin wave, $\sim c$ from (27). As expected, this wave only propagates to the east. From the measured zonal phase speed in figure 6(*b*), $c_m = 4.1\ \mathrm{cm\ s}^{-1}$, the 'measured' Lamb parameter $\epsilon_m = 39$. Even at this intermediate value, the wave dynamics is that of the equatorial β-plane. The predicted Lamb parameter using the predicted magnetic gravity wave phase speed, c, of (27) is somewhat difficult to determine owing to the sensitivity of c to the difficult-to-measure magnetic field strength and gradient. As shown below, $c > c_m$ and therefore $\epsilon < \epsilon_m$, but differ by factor of 2 or less.

Longuet-Higgins (1968, referred to herein as L-H) gives analytic approximations to the full numerical solution to the Laplace tidal equations in the limits of large or small Lamb parameter. While these experiments are not truly spherical as required by the Laplace tidal equations, in the limit of large ϵ the fluid motions are predicted and observed to be trapped at equatorial latitudes where the magnetic potentials and resultant force (figure 4) is nearly spherically symmetric. For large ϵ the waves are of three types given in L-H §8. The low-frequency and low-zonal-wavenumber waves

correspond to the solutions on the equatorial β-plane with the latitude coordinate written $\xi = \epsilon^{1/4} \sin\theta$ where θ is the latitude in L-H, or $\xi = y/L_{eq}$ where y is the northward coordinate on the equatorial β-plane (in Philander 1990, §3.4, for example). For large ϵ, the L-H type 3 eastward wave (Kelvin wave) has the form

$$u \propto \frac{2\epsilon^{3/4}}{n} \, \mathrm{e}^{-\xi^2/2} \, \mathrm{e}^{\mathrm{i}(n\theta-\omega t)}, \quad v \propto \mathrm{i}\xi \, \mathrm{e}^{-\xi^2/2} \, \mathrm{e}^{\mathrm{i}(n\theta-\omega t)}, \quad \eta \propto \frac{2\epsilon^{3/4}}{n} \frac{D}{c} \, \mathrm{e}^{-\xi^2/2} \, \mathrm{e}^{\mathrm{i}(n\theta-\omega t)} \quad (28\,a\text{–}c)$$

(L-H equations 8.40–8.42). In the equatorial β-plane limit, $\epsilon \to \infty$, (28) become the standard equatorial Kelvin wave with Gaussian u and η, and $v \to 0$ (Philander 1990, equation 3.48). The waves have a dispersion relation (L-H equation 8.38):

$$\omega/k = c(1 + \tfrac{1}{4}\epsilon^{-1/2}), \tag{29}$$

where $n = kR$. For $\epsilon \to \infty$, (29) reduces to non-dispersive Kelvin waves travelling at the shallow-water wave speed, (27) for this ferrofluid system. The westward solutions of type 2 in L-H are the Rossby waves on the equatorial β-plane (L-H equations 8.35–8.37):

$$u \propto \frac{2m+1}{2n} \, \epsilon^{1/4} \, \mathrm{e}^{-\xi^2/2} \left(P_{m-1}(\xi) - \frac{1}{2m+2} \, P_{m+1}(\xi) \right) \mathrm{e}^{\mathrm{i}(n\theta-\omega t)}, \tag{30\,a}$$

$$v \propto -\mathrm{i} \, \mathrm{e}^{-\xi^2/2} P_m(\xi) \, \mathrm{e}^{\mathrm{i}(n\theta-\omega t)}, \tag{30\,b}$$

$$\eta \propto -\frac{2m+1}{2n} \, \epsilon^{1/4} \, \mathrm{e}^{-\xi^2/2} \left(P_{m-1}(\xi) + \frac{1}{2m+2} \, P_{m+1}(\xi) \right) \mathrm{e}^{\mathrm{i}(n\theta-\omega t)} \tag{30\,c}$$

(alternatively Philander 1990, equations 3.33 and 3.36) where P_m is the Hermite polynomial of degree m. In effect m is the meridional mode number as n is the zonal mode number. The zonal dispersion relation for these waves is

$$\frac{\omega}{k} = -\frac{c}{2m+1}, \tag{31}$$

so that they travel to the west at $\frac{1}{3}$, $\frac{1}{5}$, $\frac{1}{7}$, etc. of the Kelvin wave speed.

This ferrofluid system is qualitatively similar except for the latitude dependence of 'gravity' and the not quite spherical geopotentials. The eigenfunctions of the equivalent Laplace tidal equations for the magnetic geopotentials could be found in the same way as in L-H, but is beyond the scope of this paper. For sufficiently large rotation and therefore ϵ, the extratropical dynamics can be ignored since waves are trapped at the equator. The decrease of $\boldsymbol{\nabla}|H|$ with increasing latitude in figure 4(*b*) does imply a decrease of wave phase speed with latitude which is compensated somewhat by the increase of ferrofluid depth with increasing latitude. In the WKB sense wave rays are therefore refracted away from the equator. In these experiments the equatorial trapping of wave energy with increasing ϵ must overcome this anti-waveguide effect as well. These experiments have Lamb parameters from order 1 to 320. At low ϵ the meridional structure and speed of the waves can be at least qualitatively compared to the L-H solutions of the Laplace tidal equations. For large enough ϵ, we expect correspondence to (28)–(31). From figure 4(*b*) for latitudes within $\pm 20°$ of the equator, the force is constant with latitude to within 5% and thus the speed is constant to within 3%. An equatorial Rossby radius of 20° corresponds to $\epsilon = 73$. For the largest Lamb parameter of the experiments, $\epsilon_m \approx 320$, the Rossby radius is 13.7° and the term $\mathrm{e}^{-\xi^2/2}$ in (28) and (30) falls to 0.35 at 20° latitude. In addition, the error in phase speed by neglecting the last term in (29) is only about 1% for $\epsilon \approx 320$. Thus the equatorial latitudes in these experiments at large Lamb parameter should still be well modelled by the equatorial β-plane approximation.

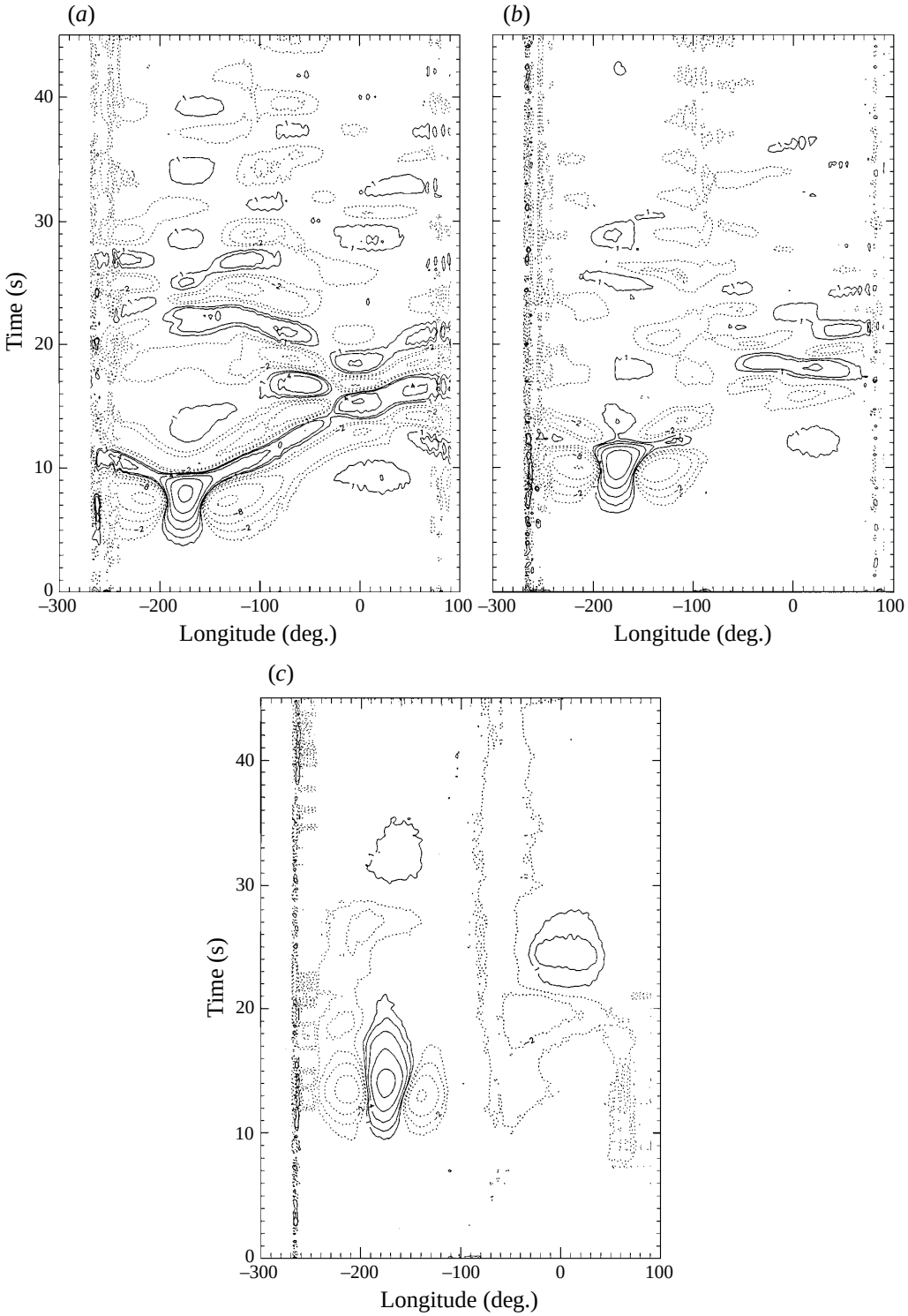

FIGURE 7. Contours of displacement height from a side view of the medium depth case as a function of latitude and time. Forcing is eastward in all cases. Latitude $-90°$ is the south pole, $0°$ is the equator on the right limb, $+90$ and $-270°$ is the north pole, and $-180°$ is the equator on the left limb. Contours are shown at $\pm 1, \pm 2, \pm 4, \pm 8, \ldots$ pixels with 1 pixel = 0.039 cm depth. (*a*) $\Omega = 0.5\ \mathrm{s}^{-1}$, $\epsilon_m = 7.1$; (*b*) $\Omega = 1.0\ \mathrm{s}^{-1}$, $\epsilon_m = 29$; (*c*) $\Omega = 2.0\ \mathrm{s}^{-1}$, $\epsilon_m = 114$.

4. Experimental results

The trapping of wave energy near the equator for rotationally dominated flows is demonstrated in figure 7. In this medium-depth case $D = 1.5$ cm, $R = 7.2$ cm, and Ω increases from 0.5 to 1.0 to 2.0 s^{-1} from 7(*a*) to 7(*c*). The video camera looks from the side as in figure 2(*b*) and waves are generated with eastward forcing which is out of the paper on the left side of figure 2. The grabbed frames are contoured and converted to polar coordinates and again plotted as displacement amplitude $r - r_0$ at each latitude as a function of time, where r_0 is the average of the first three frames. Again the height resolution of the images is about 0.1 pixel or 3.9×10^{-3} cm. In these plots latitude $-180°$ corresponds to the equator on the left limb (longitude of closest approach of the forcing magnet), $-90°$ is the South pole, 0° is the equator on the right limb, and $+90°$ or $-270°$ is the north pole where the Plexiglas rod interferes with the waves and visualization. Using the measured phase speed at $\Omega = 2.0$ s^{-1}, $c_m = 2.7$ cm s^{-1}, the Lamb parameter, ϵ_m, is 7.1, 29 and 114 in the three cases.

Kelvin waves

In figure 7(*a*) at low ϵ, much of the wave signal travels over the poles as discussed above in relation to the non-rotating case in figure 6(*a*). The three-dimensional ray paths are ambiguous using this profile-viewing technique, but other experiments with a grid projected onto the surface of the ferrofluid for visualization show that at low rotation rates, the wave crests propagate to high latitudes and over the poles. In figure 7(*c*) for $\epsilon_m = 114$, the surface height displacement propagates just zonally and disappears while propagating across the near or far hemisphere. The height displacement is visible only near the equator in this side limb view. The forced surface displacements are centred on the equator and roughly Gaussian so that eastward forcing should couple strongly to the freely propagating Kelvin wave (equation (28*c*)) at large Lamb parameter. For $\epsilon = 114$, the equatorial Rossby radius is about 18° which is roughly the half-width of the forced wave in figure 7(*c*). After propagating both one-half and one revolution of the spheroid, the travelling wave is somewhat broader latitudinally, probably owing to friction, as discussed in more detail below. Westward forcing in the side-view experiments with shallow and medium ferrofluid depths give no discernible propagating free wave.

Combining the bottom view (zonal projection) at moderate Lamb parameter of figure 6(*b*) with the side view (meridional projection) at larger ϵ of figure 7(*c*) gives a picture of an equatorially trapped Kelvin wave propagating to the east. This eastward wave appears non-dispersive in both projections. The eastward wave in the zonal projection has a steep front with high zonal wavenumber but with little or no dispersion as it travels around the spheroid. The non-dispersive, eastward-only phase speed and meridional wave-height profile are consistent with the Kelvin wave given by (28) travelling at phase speed given by (29).

Equation (29) predicts that the zonal phase speed is just the shallow water wave speed of (27). This prediction can be compared to these measurements of eastward Kelvin waves at large ϵ. The shallow-water phase speed depends on fluid depth as $D^{1/2}$ in the usual way as well as inversely to a higher power of R through both $(\nabla H)_D$ and M_D. Thus for small depth the phase speed increases with depth as $D^{1/2}$, but for larger depths the terms $\nabla H \sim (R - R_0)^{-4}$ and $M = L\{H\} \sim L\{(R - R_0)^{-3}\}$ dominate. This dependence of H on R based on (23) is only approximate in the near field of the magnet where the field actually falls off faster than for a dipole.

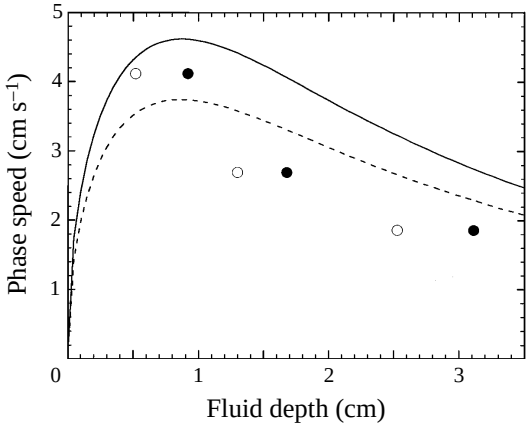

FIGURE 8. Predicted and measured zonal phase speed as a function of ferrofluid depth at the longitudes of maximum (——, predicted; ●, measured) and minimum (– – –, ○) depth which are different owing to miscentring of the plaster spheroid on the magnet. Predicted speed is from (27) based on measurements of magnetic field and ferrofluid strength.

The measurements of field *vs*. depth mentioned above were used to calculate H and ∇H as a function of depth and radius at four longitudes around the plaster ball. M_s was found using the measured density and the fit in figure 3(*b*) and then M as a function of ferrofluid depth using (11) with the fit parameters from figure 3(*a*). The resulting prediction for c for two longitudes is shown in figure 8. The magnet and plaster ball centres are displaced horizontally about 0.2 cm along the direction of the two longitudes shown in figure 8. The ferrofluid surface lies along a magnetic potential surface which is displaced by the same amount so that the fluid depth also varies as a function of longitude. The ferrofluid depths and thus the speeds shown are the extremes for a given ferrofluid volume. The three measured average Kelvin wave speeds for the three ferrofluid depth experiments are also plotted *vs*. the minimum and maximum measured depths in figure 8. The measured speed is smaller by of order 30% than that predicted by (27) for the two larger fluid depths. This corresponds to a difference of 50% in the Lamb parameters, ϵ_m and ϵ, based on the two wave speeds.

While not in quantitative agreement for all the fluid depths, the data and predictions are consistent in some important ways. Quantitatively, the phase speed prediction depends sensitively on the measurements of H and particularly ∇H. To get a continuous prediction with depth, Hall probe measurements of H *vs*. distance from the plaster sphere were fit with a polynomial which was differentiated to get ∇H. These measurements are most critical to the phase speed prediction and unfortunately are the most susceptible to systematic errors. The counter-intuitive decrease of travelling wave speed with increasing ferrofluid depth for this shallow-water wave system is verified in the experiments. Furthermore, even though the depth of the ferrofluid varies with longitude for a given experiment, the measured speed does not (e.g. figure 6*b* and figure 9*a*). In figure 8 the predicted maximum and minimum speeds are nearly equal for a given ferrofluid volume if the depth difference at the two longitudes is about 0.5 cm for depths above 1 cm. In other words even though the depth varies with longitude due to misplacement of the magnet within the plaster ball, the larger magnetic gravity at smaller depth almost exactly compensates and the speed given by (27) remains constant with longitude, consistent with the experimental result.

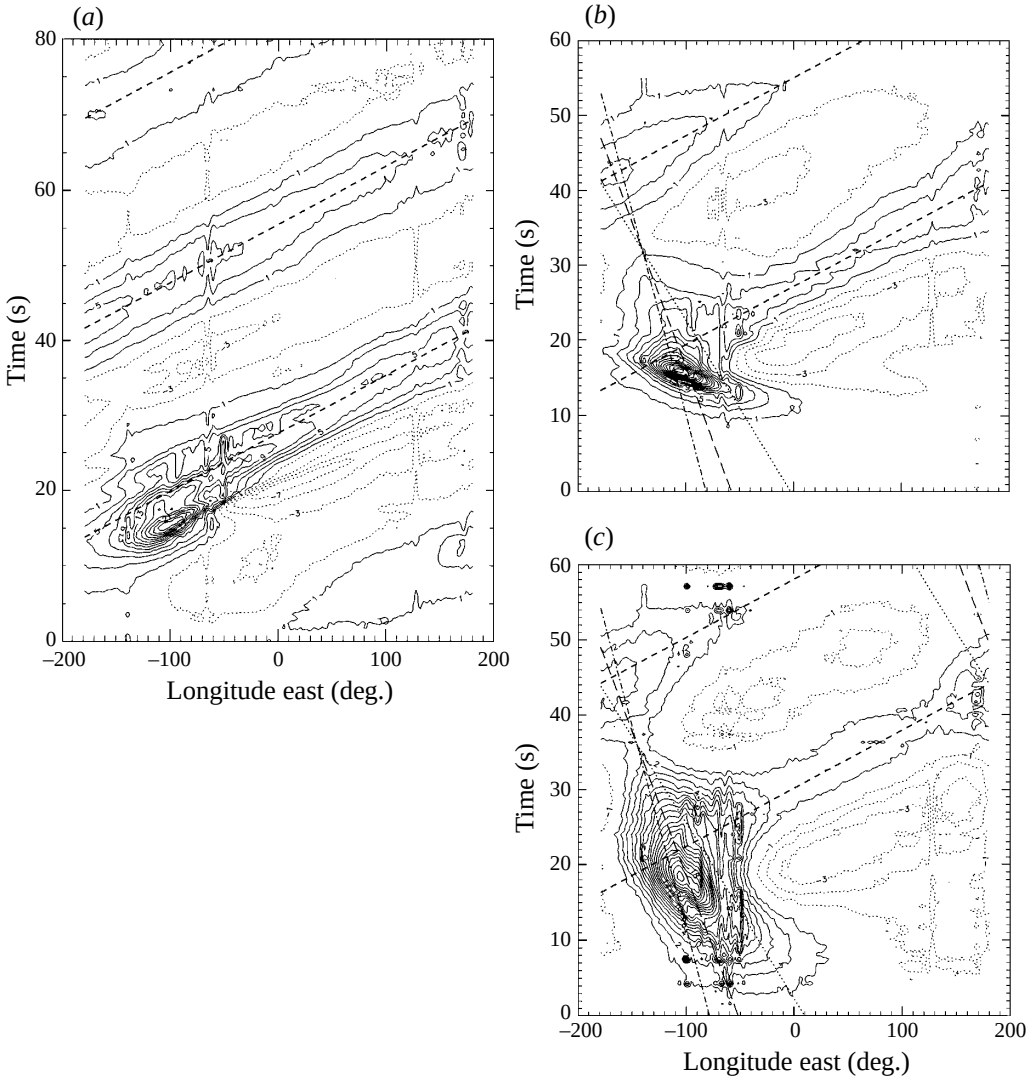

FIGURE 9. Contours of displacement height, $r-r_0$, near the equator for the deep case as a function of longitude and time. $\Omega = 2.0$. (*a*) Eastward forcing at about the Kelvin wave speed. (*b*) Westward forcing at same speed as in (*a*). (*c*) Westward forcing at 0.44 times the speed of (*b*). The eastward line (– – –) has $c_m = 1.86$ cm s^{-1} so $\epsilon_m = 330$. The lines · · ·, – – –, and – · – · correspond to westward speeds which are $\frac{1}{3}$, $\frac{1}{5}$, and $\frac{1}{7}$ of c_m, respectively.

Rossby waves

At large ϵ, or equivalently on the equatorial β-plane, we also expect westward-propagating Rossby waves with the form given by (30) travelling at phase speed given by (31). The latitudinal structure is given by Hermite polynomials within a Gaussian envelope. The lowest mode, $m = 1$, has a height signal which is symmetric about the equator with maxima off the equator and a local minimum, but still positive, height on the equator. This mode should couple most strongly to the imposed roughly Gaussian height anomaly. This $m = 1$ (the gravest equatorial Rossby) mode also has the fastest phase speed, 1/3 that of the Kelvin wave. The next mode is antisymmetric in height about the equator.

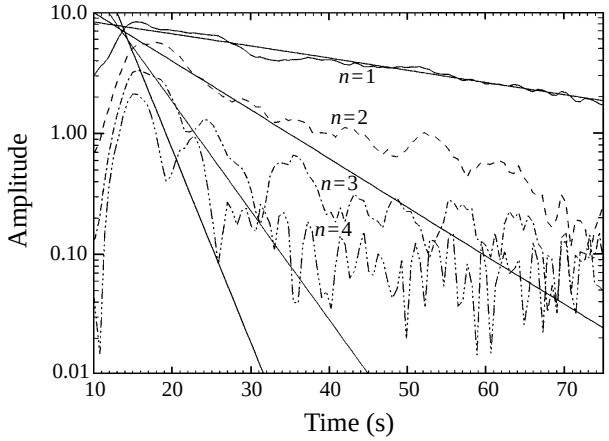

FIGURE 10. Amplitude of the lowest four zonal wavenumber components of the Kelvin wave in figure 9(*a*) as a function of time. The uppermost straight line is a fit to the $n = 1$ amplitude and gives a decay time of 43 s. The other straight lines are guides and have decay times of 4, 9, and 16 times 43 s.

For the deep ferrofluid layer experiments, the bottom drag is smaller and the ferrofluid surface is nearer to the forcing so that large waves which propagate a few times around the spheroid are possible. In figure 9(*a*) with $\Omega = 2.0\ \mathrm{s}^{-1}$ the height signal *vs*. longitude and time shows a Kelvin wave which travels around the spheroid more than twice. For this deep layer experiment c_m is measured to be $1.86\ \mathrm{cm\ s}^{-1}$ and therefore $\epsilon_m = 330$. The height resolution of 0.1 pixel now corresponds to 4.4×10^{-3} cm. As in the shallow depth case, the largest forcing amplitude occurs downstream of the forcing magnet's closest approach longitude. The wave appears non-dispersive, however the zonal wavenumber of the freely propagating wave is dominated by $n = 1$ after the forcing dies out (see also figure 10). Thus different speeds for different zonal modes would be difficult to detect. The phase speed of this wave is constant during the lifetime shown. The wave signal follows a line of constant slope and therefore velocity ($1.86\ \mathrm{cm\ s}^{-1}$) which is drawn onto the contour plot.

In figures 9(*b*) and 9(*c*) the forcing is westward at the same rotation rate. The forcing in figure 9(*b*) is at the same speed as in figure 9(*a*) and is just over twice that of figure 9(*c*). In figure 9(*b*), a small eastward Kelvin wave is still generated but now some westward propagation is visible as well. In figure 9(*c*) the slower forcing generates a Kelvin wave with yet smaller amplitude and couples better to the slower westward-propagating wave. This behaviour is reminiscent of simple numerical results of the release of a height perturbation on the equator and the subsequent generation of both eastward Kelvin and westward Rossby waves (Philander 1990 for example). Figures 9(*a*) and 9(*c*) are the laboratory analogues of recent sea surface height anomaly observations of Kelvin and Rossby waves in the Equatorial Pacific measured by Seasat (Delcroix *et al*. 1991, figures 6 and 8) and TOPEX/POSEIDON (Chelton & Schlax 1996, figure 3).

In figures 9(*b*) and 9(*c*), lines with slopes equal to $\frac{1}{3}$, $\frac{1}{5}$, and $\frac{1}{7}$ of the measured Kelvin wave speed in figure 9(*a*) are shown for reference. These speeds correspond to the first three Rossby modes (equation (31) with $m = 1$, 2, and 3). Based on latitude profiles of the forcing, we expect to generate the gravest Rossby mode with speed $\frac{1}{3}$ of the Kelvin mode. The data seem to better support a phase speed of $\frac{1}{5}$ or $\frac{1}{7}$ of the Kelvin mode. The discrepancy is probably due to the viscosity of the ferrofluid and especially the silicone oil bath.

Since the ferrofluid is a suspension of particles in a carrier fluid and these particles' orientation depends on the external magnetic field, $\boldsymbol{H}$, it is expected that the viscosity depends on both the magnitude and direction of $\boldsymbol{H}$. Rosensweig (1985) considers a ferrofluid in a plane Couette shear flow with an applied magnetic field. If the vortical rotation timescale in the fluid flow is much larger than the particle rotation time ($\tau \lesssim 10^{-6}$ s) as in these experiments, then the increase in fluid viscosity due to the magnetic field is

$$\frac{\Delta\nu}{\nu} = \frac{MH\tau/4\nu\rho}{1+MH\tau/6\nu\rho\phi}\sin^2\gamma \tag{32}$$

(Rosensweig 1985, from equation 8.100) where ϕ is the volume fraction of the magnetic particles in the ferrofluid and γ is the angle between the fluid vorticity and the magnetic field. If we estimate ϕ from the relation, $\phi = M_s/M_d$, where M_d is the bulk magnetization of the magnetite particles ($\sim 400\,\text{Gauss}/4\pi$), then $\phi \sim 0.0015$ and $\Delta\nu/\nu < 0.002\sin^2\gamma$. This effect is thus very small even in the case where the vorticity and field are perpendicular and can be ignored for this very dilute ferrofluid.

The effects of the usual fluid viscosity on the equatorial Kelvin wave can be explored with a very simple model in which the Gaussian latitude dependence is assumed unchanged. A term $\nu\nabla^2 u$ included in the $\hat{x}$-momentum equation ($v = 0$) leads to a complex frequency ω along the equator ($y = 0$) of

$$\omega = -\frac{\mathrm{i}}{\tau} + \frac{nc}{R}\left[1-\left(\frac{R}{\tau nc}\right)^2\right]^{1/2}, \tag{33}$$

where

$$\frac{1}{\tau} = \frac{\nu}{2R^2}(n^2+\epsilon^{1/2}). \tag{34}$$

Thus the wave ampitude decays like $\mathrm{e}^{-t/\tau}$ and the zonal phase speed has a correction factor multiplying the shallow-water wave speed:

$$\frac{\omega}{k} = c\left[1-\left(\frac{R}{\tau nc}\right)^2\right]^{1/2}. \tag{35}$$

In figure 10 the amplitudes of the first four zonal wavenumber components of the deep-layer Kelvin wave in figure 9(*a*) are shown as a function of time. The linear fit on the semi-log plot for the $n = 1$ wave gives a decay time of 43 s. Using these quantities in (34) along with R for the deep case and the Lamb parameter, ϵ_m, determined from the measured wave speed gives a viscosity of 0.18 $\text{cm}^2\,\text{s}^{-1}$. This is a factor of at least 3 larger than any fluid in the experiment and indicates that the assumption that the spatial structure does not change is not a good one. Similarly, for the Lamb parameter of this experiment, (34) predicts essentially no difference in τ for the $n = 1$ and $n = 2$ modes since the $\epsilon^{1/2}$ term dominates n^2. However, in figure 10, rather than staying constant, the decay times go down like n^2 for early times, again indicating that the latitudinal structure is not constant.

Using the 43 s decay time in (35) anyway to determine a correction for the predicted phase speeds of figure 8 gives a modification factor of 0.99 or essentially no change. Since the spatial structure is observed to change in figure 7 where the Kelvin mode broadens in latitude, and the decay times are much faster than this simple model predicts, we expect that a solution to the problem with spatial variations intact is required. Such a solution is not particularly interesting from a geophysical point of

view even if done on the equatorial β-plane. For the full experimental geometry, it is even more complicated. Instead we simplistically conclude that the smaller spatial scales of the Rossby waves give smaller decay times (as observed in comparing figures 9*a* and 9*c*), and that they retard the phase speed of the waves more than the Kelvin waves by an unknown but perhaps insignificant amount. The smaller meridional scale of the Rossby waves implies even more spatial broadening owing to viscosity so that a correspondingly larger correction to the phase speed seems reasonable. A much better solution to resolving the discrepancy between the observed Rossby wave speed of about $\frac{1}{5}$ the Kelvin wave speed for what is likely the lowest Rossby mode (for which we expect $\frac{1}{3}$) is to lower the viscosity of the oil bath and/or increase the size of the apparatus.

5. Conclusions

The theoretical construct of the equatorial β-plane has been successful in modelling observations of tropical waves in the atmosphere and ocean. The Kelvin and Rossby waves predicted to exist in this system have been observed in this laboratory experiment. While the observational, numerical and theoretical basis for the existence of these waves is formidable, until this set of experiments, study of this system in the laboratory had not been achieved. On a broader level, the spherical geometry of these experiments demonstrates the utility of ferrofluids and their extra body force for the generation of potential vorticity gradients which are not totally constrained by terrestrial gravity's flat geopotentials on laboratory scales. Much progress has been made using laboratory experiments which can simulate limited aspects of the full scope of geophysical fluid dynamics (i.e. a thin shell of stratified fluid flowing on a rotating sphere, driven by surface stresses and differential heating). With ferrofluids whole new classes of laboratory experiments aimed at understanding GFD become possible.

The most obvious limitation to this study of free-surface spherical shallow-water waves is the viscous damping imposed by the oil bath. For related experiments an easy but not inexpensive improvement would be to use Dow Corning's 0.0065 rather than 0.05 $\mathrm{cm^2\ s^{-1}}$ viscosity silicone oil. In addition, the magnetic force on the ferrofield is sufficiently strong that less-dilute ferrofluid could be used with larger magnets to give similar forces in larger geometries. The magnet and therefore the spheroid size can be scaled up by a factor of three while still giving similar field strengths and gradients or by a larger factor by going to smaller fields and less-dilute ferrofluid. This increase in size would reduce the viscous effects by an order of magnitude. Surface tension effects would also be reduced for larger experiments.

Using a less-viscous fluid system allows laboratory study of a wider range of geophysical flows in this nearly spherical geometry. Kelvin waves can be trapped to coastlines rather than just the equator. These trapped waves decay exponentially in the offshore direction with a lengthscale of the Rossby radius, $L_r = c/f$. For larger geometries this lengthscale can be sufficiently small that studies of equatorial waves in ocean basins which may scatter into coastal Kelvin waves as they strike the eastern ocean boundary, or studies of such waves as they propagate and scatter through island archipelagoes become possible. In the ocean these waves are the first few baroclinic modes and have decay scales which are of order 1/100 or less of the basin width. In a 20 cm radius homogeneous ferrofluid experiment the waves would be barotropic surface waves but with nearly as small a decay scale compared to the basin size. If $c \sim 2$ cm $\mathrm{s^{-1}}$, and L_r or island sizes are ~ 2 cm then the Reynolds number is order 400 and viscous effects would not be dominant. Such ocean basin experiments would still

be limited by non-geophysical viscous and surface tension effects for smaller-scale waves or topography and by the non-spherical geopotentials at high latitudes. However, large-amplitude waves are easy to generate and these experiments would have the advantage of being fully nonlinear three-dimensional real fluid systems rather than numerical or theoretical models.

Experiments which are not motivated by geophysical fluid dynamics but by geometrical constraints are possible in this nearly spherical geometry. For example a channel formed by continents at about $\pm 10°$ or 20° latitudes would have true periodic boundary conditions in the wave propagation direction. This geometry is standard for many theoretical models of wave propagation and solitons but is difficult experimentally. For capillary gravity waves for example, a standard annulus has different length sidewalls and corresponding curvature effects which complicate the surface tension terms. In this ferrofluid system the curvature would instead be in the 'gravity' direction. Similarly, capillary–gravity waves on the full sphere could be studied, without boundaries or contact angle complications. In particular, an oscillating magnetic field produced by an internal electromagnet would give an oscillating body force which might allow Faraday waves on a surface with no sidewall effects.

We have constructed ferrofluid stratifications by dilution in a number of quasi-spherical and flat geometries. From figure 3(*b*) this gives a stratification in both density and magnetization. The elimination of terrestrial gravity from the dynamics depends on having a uniform density throughout the fluids so spherical stratified experiments are not possible without free-fall or Earth orbit. Otherwise, both gravity and the magnetic body forces act inside the fluid. A stratification of the ferrofluid used in this study in a magnetic field with a strength gradient of about 20 Gauss cm^{-1} would have the same magnetic buoyancy frequency as gravitational buoyancy frequency. Stronger field gradients mean that the magnetic body force dominates and experiments with stratified dynamics whose geopotentials are not all parallel as in figure 1(*f*) become possible. Such a geometry would make a true stratified β-plane with the addition of planetary rotation. Very large field gradients with simple magnetic shapes implies small sizes and concurrent viscous effects so the geophysical applications may be limited. In addition, the fluid is very black and so internal dynamics are experimentally difficult to visualize. We have demonstrated the direct sensing of local M variations via inductance and *in situ* field strength measurements, and ultra-sound techniques may be feasible, but much work remains.

The continued motivation for conducting laboratory experiments in the light of the advances being made in numerical techniques and hardware remains the large three-dimensional dynamical ranges and evolution times available for some laboratory problems compared to numerical models. Carefully scaled laboratory experiments using ferrofluid may offer many new possibilities and geometries for studies of geophysical fluid dynamics. The recent availability of inexpensive ferrofluid (about $10 a litre for these experiments) now makes such experiments practical.

The experiments were conducted in the Geophysical Fluid Dynamics Laboratory at the School of Oceanography, University of Washington, which is partially supported by the Office of Naval Research. D. R. O. was supported by ONR grant N00014-90-J-1477 and NSF grant OCE-94-16661. P. B. R. was supported by ONR grant N00014-92-J-1405 and NSF grant OCE-93-01819. We thank Eric Lindahl for construction of the plaster spheroid and for assistance in conducting the experiments. The image processing was done using equipment in John E. Hart's GFD laboratory at the University of Colorado. We thank Ronald Rosensweig of Exxon Corp, for assistance

with obtaining and characterizing ferrofluids. We acknowledge helpful conversations with R. Hallberg and G. Dairiki. Suggestions from two anonymous referees improved the ferrofluid theory and conclusion sections of the paper.

REFERENCES

Azouni, M. A., Bolton, E. W. & Busse, F. H. 1986 Convection driven by centrifugal buoyancy in a rotating annulus. *Geophys. Astrophys. Fluid Dyn.* **34**, 301–317.

Baker, D. J. & Robinson, A. R. 1969 A laboratory model for the general ocean circulation. *Phil. Trans. R. Soc. Lond.* A **265**, 533–566.

Bashtovoy, V. G., Berkovsky, B. M. & Vislovich, A. N. 1988 *Introduction to Thermomechanics of Magnetic Fluids*. Hemisphere.

Carrigan, C. R. & Busse, F. H. 1983 An experimental and theoretical investigation of the onset of convection in rotating spherical shells. *J. Fluid Mech.* **126**, 287–305.

Chantrell, R. W., Popplewell, J. & Charles, S. W. 1978 Measurements of particle size distribution parameters in ferrofluids. *IEEE Trans. Magnetics* **MAG-14(5)**, 975–977.

Chelton, D. B. & Schlax, M. G. 1996 Global observations of oceanic Rossby waves. *Science* **272**, 234–238.

Colin de Verdiere, A. 1979 Mean flow generation by topographic Rossby waves. *J. Fluid Mech.* **94**, 39–64.

Delcroix, T., Picaut, J. & Eldin, G. 1991 Equatorial Kelvin and Rossby waves evidenced in the Pacific ocean through geosat sea level and surface current anomalies. *J. Geophys. Res.* **96** (Suppl.), 3249–3262.

Gill, A. E. 1982 *Atmosphere-Ocean Dynamics*. Academic.

Greenspan, H. P. 1968 *The Theory of Rotating Fluids*. Cambridge University Press.

Griffiths, R. W. & Cornillon, P. 1994 Laboratory experiments with mid-latitude circulation in a two-layer ocean. *Fourth Intl Symp. on Stratified Flows*, Vol. 4. Institute de Mécanique de Grenoble.

Hart, J. E. 1972 A laboratory study of baroclinic instability. *Geophys. Fluid Dyn.* **3**, 181–209.

Hart, J. E., Glatzmaier, G. A. & Toomre, J. 1986 Space-laboratory and numerical simulations of thermal convection in a rotating hemispherical shell with radial gravity. *J. Fluid Mech.* **173**, 519–544.

Holton, J. R. 1992 *An Introduction to Dynamic Meteorology*, 3rd Edn. Academic.

Ibbetson, A. & Phillips, N. A. 1967 Some laboratory experiments on Rossby waves with application to the ocean. *Tellus* **19**, 81–88.

Longuet-Higgins, M. S. 1968 The eigenfunctions of Laplace's tidal equations over a sphere. *Phil. Trans. R. Soc. Lond.* A **262**, 511–607 (referred to herein as L-H).

Matsuno, T. 1966 Quasi-geostrophic motions in equatorial areas. *J. Metl. Soc. Japan* **2**, 25–43.

Ohlsen, D. R. & Hart, J. E. 1989 The transition to baroclinic chaos on the β-plane. *J. Fluid Mech.* **203**, 23–50.

Philander, S. G. 1990 *El Niño, La Niña, and the Southern Oscillation*. Academic.

Phillips, N. A. 1966 The equations of motion for a shallow rotating atmosphere and the 'traditional approximation'. *J. Atmos. Sci.* **23**, 626–628.

Rosensweig, R. E. 1985 *Ferrohydrodynamics*. Cambridge University Press.

Salby, M. 1984 Survey of planetary scale traveling waves: the state of theory and observations. *Rev. Geophys. Space Phys.* **22**, 209–236.

Stommel, H., Arons, B. B. & Faller, A. J. 1958 Some examples of stationary planetary flow patterns in bounded basins. *Tellus* **10**, 179–187.

Taylor, G. I. 1921 Experiments with rotating fluids. *Proc. R. Soc. Lond.* A **100**, 114–121.

Whitehead, J. A. 1975 Mean flow generated by circulation on a *b*-plane: an analogy with the moving flame experiment. *Tellus* **27**, 358–3644.